Mathematical and Computational Applications

MDPI

Article

On the Numerical Solution of the Multiscale Models Characterising Noroviral Infectious Disease Systems Using the Multistage Spectral the Relaxation Method and the Nonstandard Finite Difference Method

Kizito Muzhinji

Department of Mathematical and Computational Sciences, University of Venda, P.O. Bag X5050, Thohoyandou 0950, South Africa; kizito.muzhinji@univen.ac.za

Abstract

Multiscale models for infectious disease systems are highly nonlinear. This presents substantial difficulties for both analysis and computation. Consequently, there is a continuous demand for the development of efficient numerical methods that provide reliable solutions. Over time, various numerical techniques have been developed for single-scale models. However, multiscale models have increasingly relied on built-in solvers and, more recently, the nonstandard finite difference method. The primary aim of this study is to offer an in-depth examination of the multistage spectral relaxation method (MSRM) applied to the multiscale model characterising norovirus infection. This study also provides a comprehensive comparison with the nonstandard finite difference method (NSFDM) in terms of convergence and accuracy, as well as their handling of highly nonlinear systems of ordinary differential equations. Both schemes were validated against an adaptive ODE45 scheme in MATLAB2025a, which served as the reference solver. The numerical outcomes indicate that the MSRM achieves a better accuracy level, with relative L^2 errors ranging from 10^{-9} to 10^{-7} for $\Delta\tau \leq 0.10$ and $N_{\text{ch}} = 8$. In contrast, the NSFDM provides solid first-order accuracy, yielding L^2 errors around 10^{-4}, while ensuring strict unconditional positivity and stability across all tested step sizes from $h = 0.01$ to 2.0. This study features a parameter sensitivity analysis that varies β_H, δ_H, α_h, μ_V, μ_H, as well as semi-log error graphs, convergence rate visuals, and CPU performance benchmarks. The MSRM costs about 24 times more per run, but it offers better accuracy for between-host variables. This makes it the preferred method for high-fidelity applications. In contrast, the NSFDM is the best option for quick parameter sweeps and long simulations that require guaranteed positivity.

Keywords: nonstandard finite difference method; multistage spectral relaxation method; Chebyshev–Gauss–Lobatto collocation; Gauss–Seidel linearisation; multiscale model; norovirus; positivity preservation; stiff ODE systems; parameter sensitivity

Check for updates

Academic Editor: Gianluigi Rozza

Received: 16 June 2026
Revised: 15 July 2026
Accepted: 27 July 2026
Published: 3 August 2026

Copyright: © 2026 by the author. Licensee MDPI, Basel, Switzerland. This article is an open access article distributed under the terms and conditions of the Creative Commons Attribution (CC BY) license.

1. Introduction

Mathematical modelling has become a crucial approach for comprehending the spread of infectious diseases, forecasting epidemic trends, and informing public health strategies [1]. Conventional epidemiological models typically concentrate on either the behaviour of pathogens within a host or the transmission of diseases between hosts. Nonetheless, recent advancements indicate that infectious diseases operate simultaneously across various biological levels. This necessitates modelling techniques that can integrate these

interconnected processes. Multiscale infectious disease modelling provides a framework for connecting pathogen proliferation within individual hosts to disease transmission within populations [2,3]. The theoretical basis for multiscale disease modelling relies on the replication-transmission relativity theory. This theory posits that disease dynamics arise from the interplay between microscale pathogen replication and macroscale transmission mechanisms, rather than being solely governed by a single biological scale [4,5]. Consequently, multiscale models illustrate the interaction between infection development within individual hosts and the spread of disease at the population level. This approach provides a more accurate representation of infectious disease systems compared to conventional single-scale methods [6]. These models have enhanced our comprehension of diseases such as tuberculosis and paratuberculosis. In these instances, the connections between individual infection mechanisms and population-level transmission significantly influence disease outcomes [7].

Although multiscale infectious disease models are biologically significant, they often yield coupled systems of nonlinear ordinary differential equations. These systems exhibit characteristics such as stiffness, temporal scales that vary, and strong interscale interactions [3]. Such features pose considerable computational challenges. Addressing these challenges requires numerical methods that uphold essential biological properties, including positivity, boundedness, and solution stability. When applied to stiff epidemiological systems, traditional numerical approaches like explicit finite difference and Runge-Kutta methods may lead to numerical instability, negative population figures, or incorrect long-term behaviour [8,9].

To overcome these limitations and enhance computational accuracy and efficiency, two advanced numerical approaches have emerged as promising alternatives for analysing complex infectious disease models: the multistage spectral relaxation method (MSRM) and the nonstandard finite difference method (NSFDM). MSRM integrates spectral collocation methods with iterative relaxation techniques. This method enables precise approximations and rapid convergence for nonlinear systems [10,11]. Prior research has demonstrated its efficacy in tackling complex differential systems across disciplines such as epidemiology and applied mathematics. This includes compartmental models for COVID-19 [10] and challenges in fluid dynamics [12]. MSRM can deliver exact solutions using relatively coarse computational meshes, making it a valuable approach for computationally intensive multiscale systems [13]. While NSFDM was created to maintain the essential qualitative characteristics of continuous dynamical systems through nonlocal discretisations and specific denominator functions tailored to the problem [8,14]. Unlike conventional finite difference methods, NSFDM ensures positivity, boundedness, equilibrium structures, and asymptotic stability regardless of the step size selected [8]. Its efficacy has been demonstrated across various epidemiological contexts, including models for HIV/AIDS, malaria, COVID-19, dengue fever, and Zika virus transmission [15–17]. These advantages render NSFDM particularly appropriate for long-term epidemiological simulations where biological accuracy is crucial. While there are several studies on both NSFDM and spectral relaxation techniques, to date, there is limited evidence regarding their performance in strongly coupled multiscale infectious disease models characterised by significant stiffness and nonlinear interactions across different scales. This deficiency in existing literature motivates the present study.

This paper explores the numerical solution of a multiscale norovirus in human transmission models using both MSRM and NSFDM. This study introduces an MSRM for the coupled system and assesses the two numerical approaches for accuracy, convergence, computational efficiency, robustness to step-size variations, and long-term dynamic characteristics. In addition to the Norovirus case, the proposed framework adds to the

broader field of computational epidemiology by providing insights into the effectiveness of structure-preserving and spectral-based numerical techniques for intricate multiscale infectious disease models. The contribution of the present paper is threefold: firstly, MSRM implementation for this specific nested, Holling-type-II multiscale model, including the explicit Gauss–Seidel linearisation for its particular nonlinear structure; secondly, a quantitative comparison of MSRM and NSFDM for this strongly coupled, multiscale system in terms of global error against a common ODE45 reference, step-size robustness, observed convergence order, and computational cost which, to our knowledge, has not previously been reported for a nested within-host/between-host model of this type; and thirdly, a parameter sensitivity study carried out consistently under both numerical schemes and validated against ODE45, $(\beta_H, \delta_H, \alpha_h, \mu_H)$ parameters.

The remainder of the paper is organised as follows. Section 2 presents the full Norovirus multiscale model. Section 3 develops and implements the MRSM for the coupled system. Section 4 constructs the complete NSFDM scheme and establishes its theoretical properties. Section 5 presents numerical experimental results including convergence tests, step-size sensitivity, and long-time simulations. Section 6 provides a discussion on the comparative analysis of MSRM and NSFDM.

2. Mathematical Model

Despite their biological richness, nested multiscale models present substantial analytical and numerical challenges. The coupling between scales typically introduces nonlinear terms, most commonly saturating Holling type-II or Michaelis–Menten incidence functions that render the combined system stiff, high-dimensional, and susceptible to qualitatively incorrect behaviour (including spurious oscillations and negative solutions) when discretised by standard explicit methods [18,19]. These difficulties are amplified in the multiscale setting, where fast within-host timescales coexist with slow between-host dynamics, demanding numerical schemes that are simultaneously accurate, unconditionally stable, and dynamically consistent with the biological constraints of non-negativity and boundedness of solutions [20,21].

In the present work, we study the three-dimensional nested multiscale ODE model introduced by [22], hereafter referred to as the *Norovirus model*. The model tracks the dynamics of a susceptible host population $S_H(t)$, an infected host population $I_H(t)$, and a between-host viral load $V_H(t)$ governed by the system:

$$\begin{cases} \dfrac{dS_H}{dt} = \Lambda_H - \dfrac{\beta_H S_H V_H}{P_0 + V_H} - \mu_H S_H, \\ \dfrac{dI_H}{dt} = \dfrac{\beta_H S_H V_H}{P_0 + V_H} - (\delta_H + \mu_H) I_H, \\ \dfrac{dV_H}{dt} = N_h \, \alpha_h \, I_H - \mu_V V_H, \end{cases} \tag{1}$$

subject to non-negative initial data $(S_H(0),\, I_H(0),\, V_H(0)) = (S_0,\, I_0,\, V_0) > 0$. The force of infection $\frac{\beta_H V_H}{P_0 + V_H}$ is a saturating Holling type-II functional form, where P_0 is the viral half-saturation constant. The composite coupling parameter N_h quantifies the net viral output per infected host derived from within-host equilibrium quantities [22]:

$$N_h = \frac{b_1 + \sqrt{b_1^2 + 4 b_0 b_2}}{2 b_0}, \tag{2}$$

where the coefficients b_0, b_1, and b_2 are explicit functions of the within-host parameters (see Equations (4) and (5) below), and

$$R_0 = \frac{N_e\,\alpha_e\,\Lambda_e\,\mu_c\,\beta_e}{\mu_e\,(\mu_e+\alpha_e)(\phi_t\Lambda_c+\mu_h\mu_c+\mu_c\alpha_h)} \tag{3}$$

is the within-host basic reproduction number. Following the derivation in Maphiri et al. [22], the auxiliary coefficients are:

$$\begin{cases} b_0 = \beta_e\,\rho_c\,(\mu_c+\alpha_e)(\mu_h+\alpha_h), \\ b_1 = (\mu_e+\alpha_e)(\beta_e a_0-\mu_e a_1)+N_e\,\alpha_e\,\Lambda_e\,\beta_e\,\rho_c, \\ b_2 = a_2\,\mu_c\,(\mu_e+\alpha_e)(R_0-1), \end{cases} \tag{4}$$

and

$$\begin{cases} a_0 = \phi_t\Lambda_c+\mu_h\mu_e+\alpha_h\mu_c, \\ a_1 = (\mu_h+\alpha_h)\,\rho_c, \\ a_2 = \phi_t\Lambda_c+(\mu_h+\alpha_h)\,\mu_c. \end{cases} \tag{5}$$

For a complete derivation of system (1) from its within-host and between-host components, and for the mathematical analysis including equilibrium existence, stability theory, and bifurcation results, we refer the reader to [22] and the references cited therein.

The primary objective is to examine how the within-human scale parameters influence the between-host variables concerning the infection of norovirus; for this reason, these numerical results/solutions are very important from a practical point of view. We illustrate the influence of norovirus transmission and replication parameters, which were chosen based on their significance, on sensitivity analysis on the nested model variables (S_H, I_H, V_H). The figures are plotted using parameters in Table 1 below, and the following initial values are used: $S_H = 500, I_H = 10; V_H = 300$.

Table 1. Model parameter values used for simulations [22].

Parameter	Parameter Description	Value	Units	Source
Λ_H	Supply rate of recruited humans	0.05	people day^{-1}	Assumed
N_e	Number of viruses produced through replication	100	day^{-1}	Assumed
β_H	Infection rate of humans	0.3	virus day^{-1}	[23]
δ_H	Natural death rate of humans	0.076	day^{-1}	Assumed
μ_H	Natural death rate of humans	0.076	day^{-1}	Assumed
δ_H	Infection induced death rate of humans	0.076	day^{-1}	Assumed
P_0	Viral half-saturation constant	1×10^8 [1×10^7–5×10^8]	day^{-1}	Assumed
α_h	Shedding rate of Norovirus	0.05	day^{-1}	[23]
μ_V	Natural decay rate of Norovirus	0.0667	day^{-1}	[24]
α_e	Viral replication rate at the site of infection	0.4	day^{-1}	[20]
ϕ_t	Pathogen decay rate within the host due to immune cells	0.006	day^{-1}	[20]
μ_h	Natural death rate of within-host pathogens	0.01	day^{-1}	Assumed
Λ_e	Supply rate of epithelial cells	0.07	day^{-1}	Assumed
β_e	Infection rate of susceptible epithelial cells	0.01	day^{-1}	[20]
μ_e	Natural death rate of epithelial cells	0.1	day^{-1}	[20]
Λ_c	Supply rate of immune cells	0.09	day^{-1}	Assumed
ρ_c	Immune-cell activation rate	0.1	day^{-1}	[20]
μ_c	Natural death rate of immune cells	0.3	day^{-1}	[20]

3. Numerical Implementation of the Multistage Spectral Relaxation Method

In this section, the MSRM is developed for the numerical solution of the multiscale model for the Norovirus (1). Spectral collocation methods offer high-order (exponential) convergence rates for smooth solutions and have been applied to epidemic differential

equations with considerable success [25,26]. Among these, the *Spectral Relaxation Method* (SRM), introduced by [27], linearises the nonlinear equations via a Gauss–Seidel-type iteration in which each variable is updated in sequence at every spectral collocation node. The SRM was subsequently extended to the MSRM [12,28], which divides the time domain into a sequence of short subintervals (stages), applies the spectral collocation within each stage, and propagates the terminal condition of one stage as the initial condition of the next. This multistage structure overcomes the principal limitation of global spectral methods, namely, the loss of accuracy over long time horizons for non-periodic, non-analytic dynamics, while retaining the high convergence order within each stage. The MSRM has been applied successfully to a variety of nonlinear ODEs arising in fluid mechanics, chemical kinetics, and biomathematics [11,28,29]. The MSRM greatly simplifies the highly nonlinear system of first-order initial value problems into a system of algebraic equations. We numerically implement the MSRM for the system (1) following the steps developed in [10,12,28]. The multiscale model (1) is reformulated as

$$\frac{dx_1}{dt} = \Lambda_H - \frac{\beta_H x_1 x_3}{P_0 + x_3} - \mu_H x_1, \tag{6}$$

$$\frac{dx_2}{dt} = \frac{\beta_H x_1 x_3}{P_0 + x_3} - (\delta_H + \mu_H) x_2, \tag{7}$$

$$\frac{dx_3}{dt} = N_h \alpha_h x_2 - \mu_V x_3. \tag{8}$$

replacing the variables $(S_H,\ I_H,\ V_H)$ by the variables $(x_1(t),\ x_2(t),\ x_3(t))$, respectively. The system (6)–(8) can be expressed as follows

$$\mathbf{x}' = A\mathbf{x} + N(\mathbf{x}), \tag{9}$$

where $\mathbf{x}(t) = [x_1(t),\ x_2(t),\ x_3(t)]$, and the matrix $A = a_{ij},\ \ i, j = 1, 2, 3$ is given by

$$\mathbf{A} = \begin{pmatrix} -\mu_H & 0 & 0 \\ 0 & -(\delta_H + \mu_H) & 0 \\ 0 & N_h \alpha_h & -\mu_V \end{pmatrix}, \tag{10}$$

and the vector of nonlinear components (and constant source) of the Equation (9) given by

$$\mathbf{N} = \begin{pmatrix} \Lambda_H - \frac{\beta_H x_1 x_3}{P_0 + x_3} \\ \frac{\beta_H x_1 x_3}{P_0 + x_3} \\ 0 \end{pmatrix}.$$

The Chebyshev spectral method estimates the functions using the truncated series of Chebyshev orthogonal polynomials. The Chebyshev spectral method is the cornerstone of the MSRM. The Chebyshev polynomials of order m are as follows

$$T_m(\xi) = \cos(m \cos^{-1}(\xi)), \qquad m \in \mathcal{N}. \tag{11}$$

The Chebyshev interpolation, $w_{N_{\text{ch}}}(\xi)$ at $\xi = \xi_i$ of a function $w(\xi)$ is given by

$$w_{N_{\text{ch}}}(\xi) = \sum_{i=0}^{N_{\text{ch}}} w_i L_i(\xi). \tag{12}$$

The $(N_{\text{ch}} + 1)$ Chebyshev–Gauss–Lobatto (CGL) nodes are applied as collocation points ξ_i from the extreme point of $T_{N_{\text{ch}}}(\xi)$ such that

$$\{\xi_i\}_0^{N_{\text{ch}}} = \{\cos\left(\frac{\pi i}{N_{\text{ch}}}\right) \quad i = 0, 1, \ldots, N_{\text{ch}}\}. \tag{13}$$

The justification is that the error is reduced when the Lagrangian interpolation points are considered to be the extrema of $T_{N_{ch}}(\xi)$ together with the two endpoints $\xi = \pm 1$. The Lagrange polynomials $L_i(\xi), i = 0, 1, 2, \ldots, N_{\text{ch}}$ of order i based on the CGL points are formulated as

$$L_i(\xi) = \frac{(-1)^{i+1}(1-\xi^2)T_i(\xi)}{\widehat{c}_i i^2(\xi - \xi_i)}, \quad i = 0, 1, 2, \ldots, N_{\text{ch}}, \tag{14}$$

where $\widehat{c}_0 = \widehat{c}_{N_{\text{ch}}} = 2, \widehat{c}_i = 1$, for $i = 0, 1, 2, \ldots, N_{\text{ch}}$.

$$\frac{dw(\xi)}{d\xi} = \sum_{n=0}^{N_{\text{ch}}} w(\xi_n)\frac{d}{d\xi}L_n(\xi_n) = \sum_{n=0}^{N_{\text{ch}}} D_{in}L_i(\xi_n) = \mathbf{D}W_n, \quad i = 0, 1, 2, \ldots, N_{\text{ch}}. \tag{15}$$

where $\mathbf{D}_{in} = \frac{d}{d\xi}L_n(\xi_n)$ is the $(N_{\text{ch}} + 1) \times (N_{\text{ch}} + 1)$ Chebyshev differentiation matrix for $i, n = 0, 1, 2, \ldots, N_{\text{ch}}$. The differential matrix $\mathbf{D}$ has entries:

$$\mathbf{D}_{in} = \begin{cases} \frac{\widehat{c}_i(-1)^{i+j}}{\widehat{c}_j\xi_i - \xi_j} & (i \neq n), \\ -\frac{\xi_i}{2(1-\xi_i^2)} & (i = n) \neq 0, N_{\text{ch}}, \\ \frac{2N_{\text{ch}}^2+1}{6} & i, n = 0, \\ -\frac{2N_{\text{ch}}^2+1}{6} & i, n = N_{\text{ch}}. \end{cases} \tag{16}$$

The solution process of the Equation (9) involves firstly decomposing the interval $[0, T]$ into M subinterval of equal length $\Delta\tau = \frac{T}{M}$, each given by $T_k = [t_{k-1}, t_k]$, $k = 1, 2, \ldots, M$ with the property

$$[0, T] = \bigcup_{k=1}^{M} [t_{k-1},\, t_k], \qquad t_k = k\,\Delta\tau, \quad k = 0, 1, \ldots, M.$$

Firstly, we transform the time subinterval $[t_{k-1}, t_k]$ to the interval $[-1, 1]$ on which the spectral method is defined using the transformation

$$\widehat{t} = \frac{t_k - t_{k-1}}{2}\,\xi + \frac{t_k + t_{k-1}}{2} = \frac{\Delta\tau}{2}\,\xi + \frac{t_k + t_{k-1}}{2}, \qquad \xi \in [-1, 1],$$

in each interval which is the domain of the CGL in Equation (13). The derivatives of Equation (9) are estimated using the Chebyshev differentiation matrix, which results in a system of algebraic equations on which the solution is obtained by applying the numerical schemes in each subinterval, T_j, by using the Gauss–Seidel techniques. Let the collocation points t_j^r and the approximate solution in each interval be $X_j^r = [x_s(\xi_0^r), x_s(\xi_1^r), x_s(\xi_2^r), \ldots, x_s(\xi_{N_{\text{ch}}}^r)]^T$. To achieve the algebraic system of equations, we replace the first derivatives by the Chebyshev differential matrix. The resulting algebra is as follows:

$$\left(\frac{2N_{\text{ch}}}{T}\mathbf{D} - l_{q,q}\mathbf{I}\right)X_q^j - \sum_{i=1, i\neq j}^{3} l_{s,i}X_i^j - N_q^j(X) = 0, \qquad q = 1, 2, 3, \tag{17}$$

where

- $\mathbf{I} \in \mathcal{R}^{(N_{ch}+1)\times(N_{ch}+1)}$ is the identity matrix.
- $l_{q,q}$ is the diagonal entry of A for equation q (i.e., the coefficient of x_q in equation q).
- $l_{q,i}$ $(i \neq q)$ is the off-diagonal entry of $\mathbf{A}$ that couples x_i into equation q.

- $\mathbf{N}_q(\mathbf{X}) = [N_q(x(\xi_0)), \ldots, N_q(x(\xi_{N_{ch}}))]^\top$ is the nonlinear residual vector evaluated at the nodes.

Application to the Equation (9). Writing (17) for each $q \in \{1, 2, 3\}$ explicitly, using the matrix $\mathbf{A}$ from (10):

Equation for $\mathbf{X}_1$ ($q = 1$):

$$\left(\frac{2}{\Delta\tau}\mathbf{D} + \mu_H\mathbf{I}\right)\mathbf{X}_1 + \mathbf{N}_1(\mathbf{X}) = \mathbf{0}, \tag{18}$$

where $\mathbf{N}_1(\mathbf{X}) = \left[\Lambda_H - \dfrac{\beta_H x_1(\xi_j)x_3(\xi_j)}{P_0 + x_3(\xi_j)}\right]_{j=0}^{N_{ch}}$.

Equation for $\mathbf{X}_2$ ($q = 2$):

$$\left(\frac{2}{\Delta\tau}\mathbf{D} + (\delta_H + \mu_H)\mathbf{I}\right)\mathbf{X}_2 + \mathbf{N}_2(\mathbf{X}) = \mathbf{0}, \tag{19}$$

where $\mathbf{N}_2(\mathbf{X}) = \left[\dfrac{\beta_H x_1(\xi_j)x_3(\xi_j)}{P_0 + x_3(\xi_j)}\right]_{j=0}^{N_{ch}}$.

Equation for $\mathbf{X}_3$ ($q = 3$):

$$\left(\frac{2}{\Delta\tau}\mathbf{D} + \mu_V\mathbf{I}\right)\mathbf{X}_3 + N_h\alpha_h\mathbf{X}_2 = \mathbf{0}. \tag{20}$$

Remark 1. *Equation* (20) *is already* linear *in* $\mathbf{X}_2$ *and* $\mathbf{X}_3$*; no linearisation is required for the viral-pool variable* V_H.

The MSRM uses a Gauss–Seidel update order: freshly computed iterates are used immediately in subsequent equations, eliminating the inter-equation lag of the Jacobi variant. That is, the nonlinear system (18)–(20) is solved by a *Gauss–Seidel* iterative linearisation. Let s denote the iterate index and $(\cdot)_{s+1}$ the new (unknown) iterate, $(\cdot)_s$ the current (known) iterate. At iteration $s + 1$, the nonlinear term is linearised by evaluating the nonlinear factor at the previous iterate:

$$\frac{\beta_H x_1 x_3}{P_0 + x_3} \approx \underbrace{\frac{\beta_H x_3^{(s)}}{P_0 + x_3^{(s)}}}_{\text{known coefficient}} \cdot x_1^{(s+1)}. \tag{21}$$

The vector $\boldsymbol{\phi}^{(s)}$ defined in Equation (31) is used to construct the diagonal matrix

$$\boldsymbol{\Phi}^{(s)} = \operatorname{diag}\left(\boldsymbol{\phi}^{(s)}\right) = \operatorname{diag}\left(\frac{\beta_H x_3^{(s)}(\xi_j)}{P_0 + x_3^{(s)}(\xi_j)}\right)_{j=0}^{N_{\text{ch}}}. \tag{22}$$

Consequently, the linearised infection term at the collocation nodes may be written compactly as

$$\boldsymbol{\Phi}^{(s)}\mathbf{X}_1^{(s+1)}.$$

Substituting this representation into the collocation systems (18)–(20) produces the three sequential Gauss–Seidel updates described below.

1. *Step 1—Update* $\mathbf{X}_1^{(s+1)}$.

Substituting the linearisation (21) and the diagonal matrix (22) into (18) gives

$$\underbrace{\left(\frac{2}{\Delta\tau}\mathbf{D}+\mu_H\mathbf{I}+\mathbf{\Phi}^{(s)}\right)}_{\mathbf{A}_1^{(s)}}\mathbf{X}_1^{(s+1)}=\Lambda_H\mathbf{e}, \tag{23}$$

where $\mathbf{e}=[1,1,\ldots,1]^\top\in\mathbb{R}^{N_{\text{ch}}+1}$ is the vector of ones. Thus, $\Lambda_H\mathbf{e}$ represents the recruitment term at every collocation node.

The initial condition $x_1(t_{k-1})=S_{k-1}$ is imposed at $\xi_{N_{\text{ch}}}=-1$ by replacing the last row of $\mathbf{A}_1^{(s)}$ with $\mathbf{e}_{N_{\text{ch}}+1}^\top$ and replacing the corresponding entry of the right-hand side by S_{k-1}.

2. *Step 2—Update* $\mathbf{X}_2^{(s+1)}$.

Using the freshly computed vector $\mathbf{X}_1^{(s+1)}$, the second collocation equation becomes

$$\underbrace{\left(\frac{2}{\Delta\tau}\mathbf{D}+(\delta_H+\mu_H)\mathbf{I}\right)}_{\mathbf{A}_2}\mathbf{X}_2^{(s+1)}=\mathbf{\Phi}^{(s)}\mathbf{X}_1^{(s+1)}. \tag{24}$$

The use of $\mathbf{X}_1^{(s+1)}$, rather than $\mathbf{X}_1^{(s)}$, reflects the Gauss–Seidel update order.

The initial condition $x_2(t_{k-1})=I_{k-1}$ is imposed at $\xi_{N_{\text{ch}}}=-1$ by replacing the last row of $\mathbf{A}_2$ and the corresponding right-hand-side entry.

3. *Step 3—Update* $\mathbf{X}_3^{(s+1)}$.

The third equation is linear and therefore requires no additional linearisation. Using the newly computed vector $\mathbf{X}_2^{(s+1)}$, one obtains

$$\underbrace{\left(\frac{2}{\Delta\tau}\mathbf{D}+\mu_V\mathbf{I}\right)}_{\mathbf{A}_3}\mathbf{X}_3^{(s+1)}=N_h\alpha_h\mathbf{X}_2^{(s+1)}. \tag{25}$$

The initial condition $x_3(t_{k-1})=V_{k-1}$ is imposed at $\xi_{N_{\text{ch}}}=-1$ in the same manner.

Remark 2. *The coefficient matrix* $\mathbf{A}_3$ *does not depend on the iterate, so it can be* factorised once *per sub-interval and reused across all s. Similarly,* $\mathbf{A}_2$ *is iterate-independent and can be pre-factorised. Only* $\mathbf{A}_1^{(s)}$ *changes between iterates due to* $\Phi^{(s)}$.

With the following full compact matrices, the three-step Gauss–Seidel MSRM update within each sub-interval k may be summarised compactly as

$$\mathbf{A}_1^{(s)}=\frac{2}{\Delta\tau}\mathbf{D}-\mu_H\mathbf{I}-\Phi^{(s)}, \qquad \mathbf{B}_1^{(s)}=-\Lambda_H\,\mathbf{e}, \tag{26}$$

$$\mathbf{A}_2=\frac{2}{\Delta\tau}\mathbf{D}-(\delta_H+\mu_H)\mathbf{I}, \qquad \mathbf{B}_2^{(s+1)}=-\mathbf{\Phi}^{(s)}\mathbf{X}_1^{(s+1)}, \tag{27}$$

$$\mathbf{A}_3=\frac{2}{\Delta\tau}\mathbf{D}-\mu_V\mathbf{I}, \qquad \mathbf{B}_3^{(s+1)}=-N_h\alpha_h\,\mathbf{X}_2^{(s+1)}. \tag{28}$$

Each linear system is solved by direct (LU) factorisation. The approximate solution of the system on $[0,T]$ is given by

$$X_q=\bigcup_{j=1}^{n}X_q^j(N_{ch}^J). \tag{29}$$

The Gauss–Seidel iteration within sub-interval k is terminated when

$$\max_{q\in(1,2,3)} \| X_q^{s+1} - X_q^s \|_\infty < \epsilon_{tol}, \tag{30}$$

where a typical tolerance is $\epsilon_{tol} - 10^{-10}$.

For the k-th sub-interval ($k \geq 1$), the initial conditions are the terminal values carried over from the previous sub-interval:

$$x_q^{(k)}(t_{k-1}) = x_q^{(k-1)}(\xi_{N_{ch}}), \quad q = 1,2,3.$$

The MSRM algorithm for the Norovirus multiscale model is presented in the following Algorithm 1.

Algorithm 1 MSRM Algorithm for the Norovirus Multiscale Model [28]

Input: T, M, N_{ch}, ε_{tol}, (S_H^0, I_H^0, V_H^0), model parameters. **Pre-computation (once):**

1. Compute CGL nodes $\{\xi_i\}_{i=0}^{N_{ch}}$ using Equation (11).
2. Assemble differentiation matrix $\mathbf{D}$ using Equation (16).
3. Set $\Delta\tau = T/M$.
4. Pre-factorise $\mathbf{A}_2 = \frac{2}{\Delta\tau}\mathbf{D} - (\delta_H + \mu_H)\mathbf{I}$ and $\mathbf{A}_3 = \frac{2}{\Delta\tau}\mathbf{D} - \mu_V\mathbf{I}$ (LU decomposition).

Time-marching loop ($k = 1, \ldots, M$):

1. **Initialise:** Set $\mathbf{X}_q^{(0)} = x_q(t_{k-1}) \cdot \mathbf{e}$ for $q = 1,2,3$.
2. **Iterate** ($s = 0,1,2,\ldots$):
   (a) Compute $\Phi^{(s)} = \text{diag}\left(\frac{\beta_H x_3^{(s)}(\xi_j)}{P_0 + x_3^{(s)}(\xi_j)}\right)$.
   (b) Form $\mathbf{A}_1^{(s)} = \frac{2}{\Delta\tau}\mathbf{D} - \mu_H\mathbf{I} - \Phi^{(s)}$ and set $\mathbf{B}_1^{(s)} = -\Lambda_H\mathbf{e}$; enforce boundary condition at row N_{ch}.
   (c) Solve $\mathbf{A}_1^{(s)}\mathbf{X}_1^{(s+1)} = \mathbf{B}_1^{(s)}$.
   (d) Set $\mathbf{B}_2^{(s+1)} = -\Phi^{(s)}\mathbf{X}_1^{(s+1)}$; enforce BC.
   (e) Solve $\mathbf{A}_2\mathbf{X}_2^{(s+1)} = \mathbf{B}_2^{(s+1)}$ (use pre-factorised $\mathbf{A}_2$).
   (f) Set $\mathbf{B}_3^{(s+1)} = -N_h\alpha_h\mathbf{X}_2^{(s+1)}$; enforce BC.
   (g) Solve $\mathbf{A}_3\mathbf{X}_3^{(s+1)} = \mathbf{B}_3^{(s+1)}$ (use pre-factorised $\mathbf{A}_3$).
   (h) Check convergence (30); if satisfied, set $\mathbf{X}_q^{\text{conv}} \leftarrow \mathbf{X}_q^{(s+1)}$ and exit loop.
3. **Carry forward:** $x_q(t_k) = X_q^{\text{conv}}(\xi_0)$, $\quad q = 1,2,3$.

Output: Solution arrays $\{x_q(t_k)\}_{k=0}^M$ for $q = 1,2,3$.

4. Non-Standard Finite Difference Method

The NSFDM framework, introduced and systematically developed in [14,21,30], replaces the standard time derivative with a nonstandard denominator function

$$\varphi = \frac{e^{qh} - 1}{q}, \qquad q > 0, \tag{31}$$

where q is the sum of all linear decay rates in the model, and employs nonlocal discretisation of nonlinear terms. The resulting schemes are *dynamically consistent*: they exactly reproduce the fixed points of the continuous system, preserve non-negativity and boundedness for all step sizes $h > 0$, and are unconditionally stable [18,31]. Applications of NSFDM to epidemic models are abundant; see, among many others, [19,20,32]. In the multiscale setting, the NSFDM is particularly attractive because the nonlinear coupling terms introduced by the

Holling type-II incidence function and the viral shedding term are handled exactly within the nonlocal discretisation framework without any step-size restriction.

The dynamics of the coupled multiscale model system were investigated using the NSFDM, following the procedures and rules established by [14,30]. Let

$$X^k = \left[S_H^k,\ I_H^k,\ V_H^k\right]^T$$

be the sequence of solutions which must be non-negative and satisfy the underlying biological properties of the food-borne disease multiscale model for $k \in \mathbb{N}$ and time step size $h = \Delta t$.

The NSFDM is designed so that it satisfies the conservation law property proposed by [14,30]. Define the auxiliary force-of-infection terms

$$\lambda_H^k = \frac{\beta_H V_H^k}{P_0 + V_H^k}, \tag{32}$$

The NSFDM, which approximates the norovirus disease multiscale model system (1) is then given by the following three update equations:

$$\begin{aligned} S_H^{k+1} &= \frac{\varphi(h)\,\Lambda_H + S_H^k}{1 + \varphi(h)\,\mu_H + \varphi(h)\,\lambda_H^k}, \\ I_H^{k+1} &= \frac{\varphi(h)\,\lambda_H^k\,S_H^{k+1} + I_H^k}{1 + \varphi(h)\,(\mu_H + \delta_H)}, \\ V_H^{k+1} &= \frac{V_H^n + \varphi_{V_H}\,N_h\,\alpha_h\,I_H^{n+1}}{1 + \varphi_{V_H}\,\mu_V}, \end{aligned} \tag{33}$$

The nonstandard denominator function is defined as

$$\varphi(h) = \frac{e^{qh} - 1}{q}, \tag{34}$$

where q is the *unified denominator parameter* given by the sum of all linear decay rates in the model:

$$q = \mu_H + \delta_H + \mu_V \tag{35}$$

The application of the denominator function described in Equation (34), together with the nonlocal treatment of the nonlinear terms in Equation (33), enables the NSFDM to retain the key qualitative features of the continuous system [14,21,31,33]. In particular, the method ensures positivity, meaning that all state variables remain non-negative for every $k \geq 0$ and any time step $h > 0$. This preservation maintains their biological significance as population densities and concentrations of pathogens. Furthermore, the approach demonstrates dynamic consistency. It effectively captures the primary dynamical properties of the original model, including the disease-free and endemic equilibria, as well as the threshold behaviour determined by the basic reproduction number R_0. In contrast to conventional explicit Euler-type methods, the NSFDM eliminates strict stability constraints on the time step and maintains stability for all ($h > 0$). Furthermore, this scheme preserves the underlying structure by adhering to the fundamental algebraic relationships of the continuous model, including the conservation of the total host population. Additionally, the numerical solutions remain within the positively invariant feasible region, reflecting the dynamics of the continuous system. These characteristics render the NSFDM an effective and biologically reliable numerical framework for simulating multiscale epidemic models. To substantiate this biological reliability, we first establish that the proposed NSFDM

preserves the non-negativity of all population variables at every time step, as stated in the following proposition.

Proposition 1. *Positivity preservation*

Assume that

$$S_H^0,\ I_H^0,\ V_H^0 \geq 0,$$

that $h > 0$, $P_0 > 0$, *and that all model parameters are non-negative. Then, the NSFD scheme preserves positivity; that is,*

$$S_H^k,\ I_H^k,\ V_H^k \geq 0, \qquad k = 0, 1, 2, \ldots.$$

This property is consistent with the positivity-preserving design principles of nonstandard finite difference schemes [20,21,31].

Proof. Since $h > 0$ and $q > 0$, the denominator function satisfies

$$\phi(h) = \frac{e^{qh} - 1}{q} > 0.$$

Suppose that

$$S_H^k,\ I_H^k,\ V_H^k \geq 0.$$

Then,

$$\lambda_H^k = \frac{\beta_H V_H^k}{P_0 + V_H^k} \geq 0,$$

because $\beta_H \geq 0$, $P_0 > 0$, and $V_H^k \geq 0$.

For the susceptible-host update,

$$S_H^{k+1} = \frac{S_H^k + \phi(h)\Lambda_H}{1 + \phi(h)\left(\mu_H + \lambda_H^k\right)},$$

the numerator is non-negative, and the denominator is strictly positive. Hence, $S_H^{k+1} \geq 0$.

Similarly,

$$I_H^{k+1} = \frac{I_H^k + \phi(h)\lambda_H^k S_H^{k+1}}{1 + \phi(h)(\mu_H + \delta_H)} \geq 0,$$

because its numerator is non-negative and its denominator is strictly positive.

Finally,

$$V_H^{k+1} = \frac{V_H^k + \phi(h)N_h\alpha_h I_H^{k+1}}{1 + \phi(h)\mu_V} \geq 0.$$

Therefore,

$$S_H^{k+1},\ I_H^{k+1},\ V_H^{k+1} \geq 0.$$

Since the initial values are non-negative, mathematical induction establishes positivity for every $k \geq 0$. □

The proposition establishes positivity for the displayed discrete scheme. In contrast, no complete proof of global boundedness or asymptotic stability of the discrete equilibria is provided here. Statements concerning these properties are therefore restricted to the numerical experiments and are reported as observed behaviour rather than general theorems.

5. Numerical Results

The numerical simulations investigate the performance of the NSFDM and the MSRM in solving a multiscale model of Norovirus infection. The benchmark solution is provided by MATLAB's adaptive Runge-Kutta solver `ODE45`, which acts as a standard for assessing accuracy, convergence, stability, and computational efficiency. The model consists of three interacting biological components: susceptible host population (S_H), infected host population (I_H), and viral load (V_H). The numerical findings are presented in figures that depict the system's dynamic behaviour and the numerical characteristics of the two methods. All computations were performed in MATLAB R2025a. The reference solution used `solve_ivp` (ODE45, RelTol $= 10^{-10}$, AbsTol $= 10^{-12}$). The NSFDM used fixed step size $h = 0.01$. The MSRM used $N_{\text{ch}} = 8$ CGL nodes per sub-interval of width $\Delta\tau = 0.10$ ($M = 2000$ sub-intervals), Gauss–Seidel tolerance 10^{-8}, and at most 50 iterations per sub-interval. The simulation period was $t \in [0, 200]$ days with initial conditions $(S_H^0, I_H^0, V_H^0) = (500, 10, 300)$. Tables 2 and 3 present solution values at selected time snapshots. Table 4 reports global relative L^2 and L^∞ error norms.

Table 2. Solution values of S_H and I_H at selected time points: ODE45 reference vs. NSFDM ($h = 0.01$) vs. MSRM ($\Delta\tau = 0.1$, $N_{\text{ch}} = 8$).

t (d)	S_H (Ref)	S_H (NSFDM)	S_H (MSRM)	I_H (Ref)	I_H (NSFDM)	I_H (MSRM)
0	500.0000	500.0000	500.0000	10.0000	10.0000	10.0000
20	444.9380	444.9624	444.9380	25.2972	25.2757	25.2972
40	353.1613	353.2536	353.1613	49.8668	49.8140	49.8668
60	244.7494	244.8973	244.7494	64.1318	64.0873	64.1318
80	157.3888	157.5293	157.3888	56.5211	56.5194	56.5211
100	102.8732	102.9747	102.8732	38.7532	38.7792	38.7532
150	51.9853	52.0133	51.9853	9.2381	9.2577	9.2381
200	41.4364	41.4407	41.4364	1.7937	1.7995	1.7937

Table 3. Solution values of V_H at selected time points: ODE45 reference vs. NSFDM ($h = 0.01$) vs. MSRM ($\Delta\tau = 0.1$, $N_{\text{ch}} = 8$).

t (d)	V_H (Ref)	V_H (NSFDM)	V_H (MSRM)
0	300.0000	300.0000	300.0000
20	955.8349	954.8297	955.4462
40	2191.6942	2184.7821	2187.1220
60	3481.4240	3480.8947	3484.3466
80	3858.8681	3856.8185	3858.8413
100	3226.9170	3230.3826	3230.0374
150	1048.6718	1048.0748	1046.3070
200	226.9381	227.6197	226.9381

The results in Tables 2 and 3 show that both NSFDM and MSRM effectively mimic the ODE45 reference solutions in all three compartments. The susceptible population, (S_H), declines consistently from 500 to approximately 41.4 by day 200, indicating the persistence of infection within the population. The infected population, (I_H), increases to a peak of about 64.1 around day 60 before gradually decreasing, which is characteristic of a typical epidemic outbreak. Similarly, the viral load, (V_H), rises to a maximum of approximately 3858.9 around day 80 and subsequently declines as the number of infected individuals decreases. When the numerical solutions are compared with the ODE45 reference solution, the MSRM results exhibit excellent agreement throughout the simulation period, often matching the ODE45 values to four decimal places. The NSFDM also produces accurate approximations, although slightly larger deviations are observed, particularly in the viral

load (V_H) between days 40 and 80. For example, at day 60, the MSRM solution is virtually indistinguishable from the ODE45 result, whereas the NSFDM solution shows a marginally larger error. Nevertheless, both methods successfully capture the qualitative dynamics of the system, including the decline in susceptible individuals, the transient peak in infected individuals, and the subsequent reduction in viral load. Overall, the results demonstrate that both NSFDM and MSRM are reliable numerical approaches for solving the nonlinear multiscale models of infectious disease systems, with MSRM providing a slightly higher level of accuracy relative to the ODE45 benchmark. The global relative error norms are computed over the common fine grid $\{t_k\}_{k=0}^{N}$, $t_k = kh$, $h = 0.01$, $N = 20{,}000$, on $t \in [0, 200]$ (that is the NSFDM grid), with

$$\|e\|_2 = \frac{\left(\sum_{k=0}^{N} \left(x_{\text{ref}}(t_k) - x_{\text{num}}(t_k)\right)^2\right)^{1/2}}{\left(\sum_{k=0}^{N} x_{\text{ref}}(t_k)^2\right)^{1/2}}, \qquad \|e\|_\infty = \frac{\max_{0\le k\le N} \left|x_{\text{ref}}(t_k) - x_{\text{num}}(t_k)\right|}{\max_{0\le k\le N} \left|x_{\text{ref}}(t_k)\right|},$$

where x_{ref} is the ODE45 solution (interpolated by `deval/ode45`'s dense output onto the common grid), and $x_{\text{num}} \in \{\text{NSFDM}, \text{MSRM}\}$. Because MSRM does not naturally produce values on the uniform $h = 0.01$ grid (its internal nodes are the CGL points within each $\Delta\tau = 0.1$ sub-interval), MSRM values are evaluated on the common grid using the Chebyshev interpolant of Equation (12) local to the sub-interval containing t_k, *not* by nearest-node lookup; we now state this explicitly, since it materially affects the reported errors. We also note explicitly that both norms are *relative* (normalised by the corresponding norm of the reference solution.

The analysis of errors presented in Table 4 supports the findings from the solution profiles and highlights the performance disparities between the two numerical approaches. The MSRM demonstrates significantly lower errors for all state variables. For the susceptible population (S_H), the (L^2) error is approximately (3.24×10^{-9}), in contrast to the NSFD method, which exhibits an error of (3.48×10^{-4}), representing an improvement of nearly five orders of magnitude. Comparable patterns are also observed for the infected population (I_H) and the viral load (V_H). The distinction between the two methods becomes more apparent when examining the (L^∞) norm, which quantifies the maximum pointwise error. For the viral load (V_H), the NSFDM exhibits a maximum error of approximately (3.46). Conversely, the MSRM achieves a maximum error of only (7.69×10^{-3}), indicating an improvement of nearly three orders of magnitude. This observation implies that the NSFDM tends to produce its largest errors during periods of rapid changes in the viral compartment, particularly near the peak of the infection dynamics. Despite these differences, both techniques yield bounded and qualitatively precise solutions that reflect the essential characteristics of the model dynamics. This indicates that the NSFD scheme is a robust and reliable numerical method for addressing the nonlinear HIV infection model. On the other hand, the MSRM, which employs a Chebyshev-based spectral framework with an effective step size of $(\triangle t = 0.1)$ and $(N_{ch} = 8)$, provides significantly greater accuracy. Consequently, MSRM is the preferred approach when accurate numerical approximations are required.

Table 4. Global relative L^2 and L^∞ errors vs. ODE45 reference.

Var.	NSFDM $\|e\|_2$	MSRM $\|e\|_2$	NSFDM $\|e\|_\infty$	MSRM $\|e\|_\infty$
S_H	3.4812×10^{-4}	3.2389×10^{-9}	1.5189×10^{-1}	1.1180×10^{-5}
I_H	7.7839×10^{-4}	7.1052×10^{-8}	5.6406×10^{-2}	9.8829×10^{-5}
V_H	7.9748×10^{-4}	9.0922×10^{-8}	3.4554×10^{0}	7.6879×10^{-3}

Figure 1 illustrates the temporal changes in susceptible cells, infected cells, and viral load as obtained from NSFDM, MSRM, and ODE45. The outcomes from both NSFDM and MSRM closely align with the reference solutions from ODE45. This demonstrates that both approaches can effectively represent the biological dynamics associated with Norovirus infection. Initially, the population of susceptible cells declines due to the viral infection and then stabilises at a steady-state level. Concurrently, the infected cell population experiences a temporary increase before reaching a steady state. The viral load initially rises and then reaches a plateau. A visual assessment indicates that the MSRM solution is almost indistinguishable from the ODE45 solution throughout the simulation duration, reflecting a high level of accuracy. NSFDM also accurately captures the qualitative dynamics while ensuring all state variables remain positive. These results validate that both methods uphold the biological properties of the model and deliver dependable approximations. The close agreement of the three solution profiles demonstrates that both numerical methods accurately reproduce the reference dynamics.

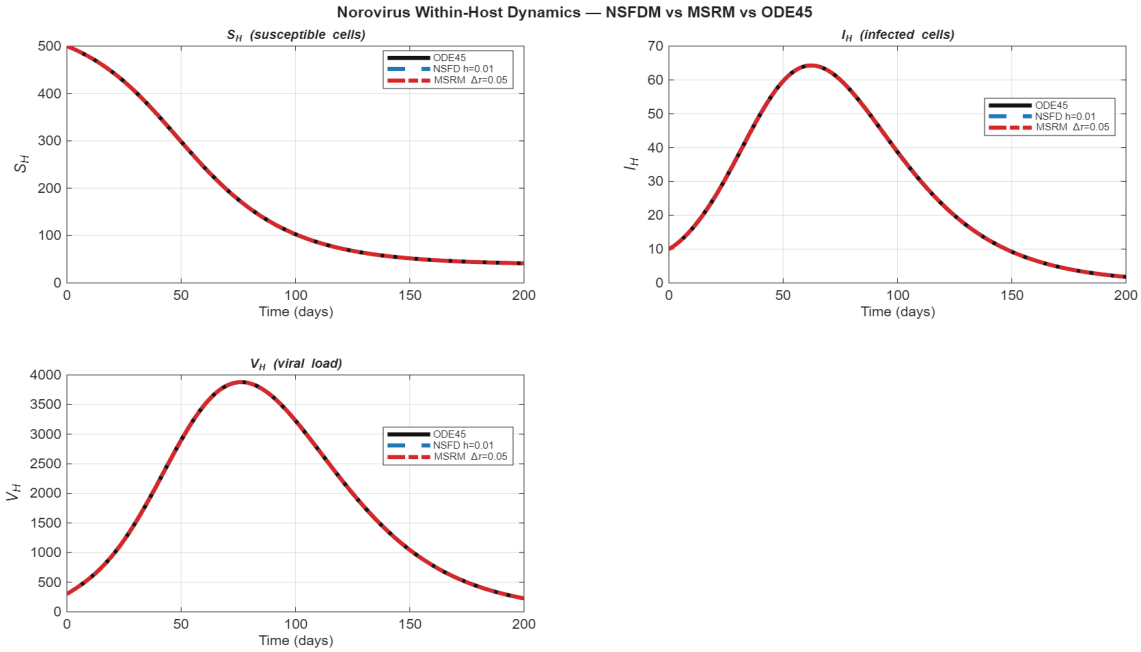


Figure 1. Numerical solutions for S_H, I_H, and V_H obtained using ODE45, the NSFDM, and the MSRM. The NSFDM was implemented with $h = 0.01$, while the MSRM used $\Delta\tau = 0.10$ and $N_{\text{ch}} = 8$, confirming convergence.

Figure 2 illustrates the semi-logarithmic profiles of absolute error for NSFDM and MSRM. The error curves remain quite small throughout the entire simulation, confirming the consistency and accuracy of both methods. The error profiles for MSRM are typically lower than those for NSFDM, highlighting the superior convergence characteristics of spectral methods. There is no amplification of error over extended simulation periods, which demonstrates numerical stability. Moreover, the smooth nature of the error curves suggests that neither method produces oscillations or misleading numerical artefacts. The findings suggest that MSRM delivers greater accuracy, while NSFDM serves as a viable alternative with acceptable levels of error.

Figure 3 analyzes the stability and positivity-preserving properties of NSFDM across various step sizes. As the step size varies from $h = 0.01$ to $h = 2.0$, all state variables remain positive and within defined limits. This demonstrates a primary advantage of Mickens-type nonstandard finite difference schemes: they uphold essential qualitative characteristics of biological systems. Although larger step sizes introduce minor deviations

from the reference solution, the overall dynamic behaviour remains unchanged. There are no instances of numerical oscillations, divergence, or negative population values. The findings indicate that NSFDM exhibits strong nonlinear stability and is especially effective for epidemiological systems where maintaining positivity is crucial.

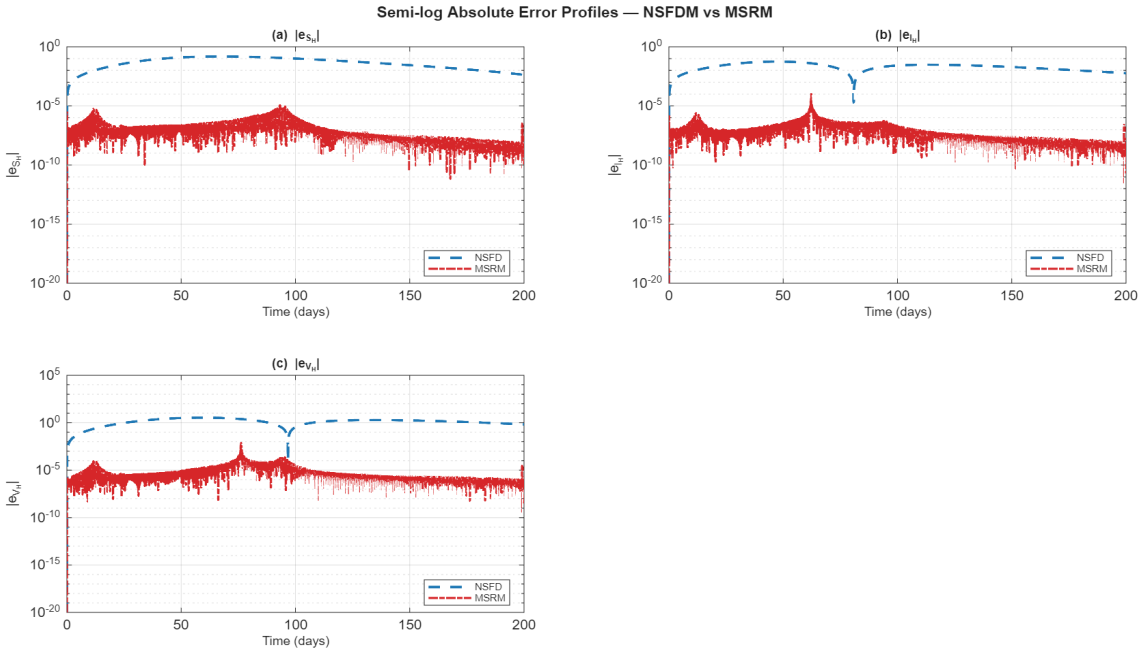


Figure 2. Semi−log absolute error profiles for S_H, I_H, and V_H, comparing NSFD ($h = 0.01$) and MSRM ($\Delta\tau = 0.1$, $N_{ch} = 8$) against the ODE45 reference over $0 \leq t \leq 200$ days. The MSRM error floor near 10^{-8}–10^{-10} reflects the Gauss–Seidel and ODE45 solver tolerances.

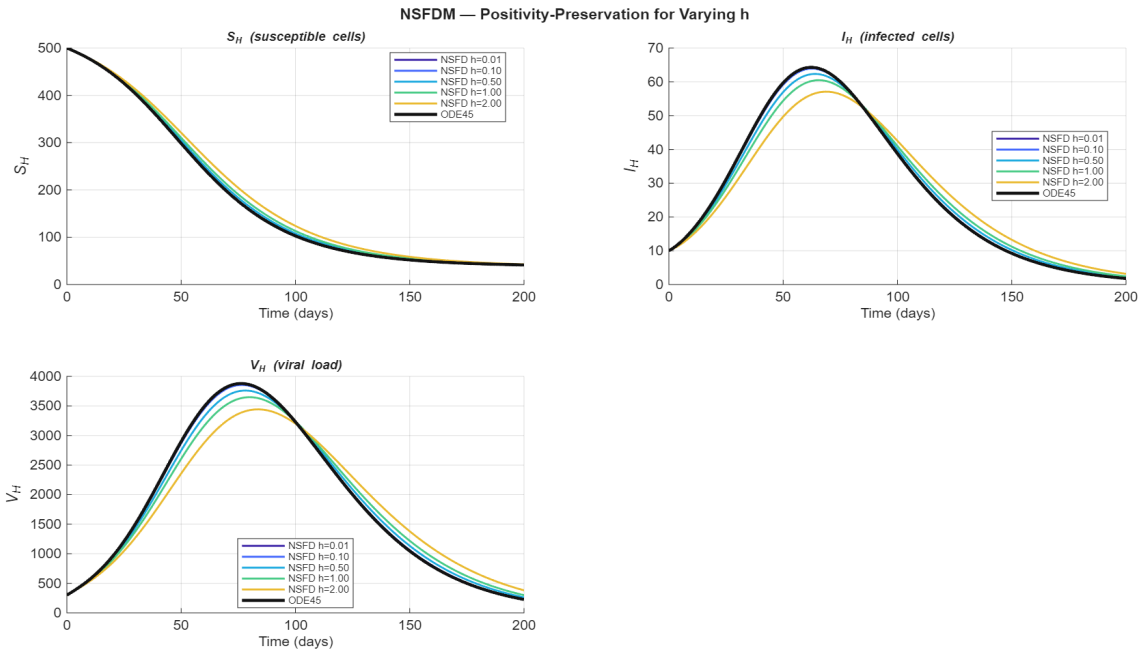


Figure 3. NSFDM solution profiles computed with step sizes $h \in \{0.01, 0.10, 0.50, 1.001, 2.00\}$ and compared with the MATLAB `ODE45` reference solution. The results illustrate the step-size sensitivity and positivity-preserving behaviour of the NSFDM.

Figure 4 illustrates the impact of reducing the size of the spectral subinterval, $\triangle t$, on the MSRM solution. As $\triangle t$ decreases, the MSRM trajectories rapidly converge to the results obtained from the ODE45 solver. Even when using relatively large subintervals,

the estimates remain highly accurate. This pattern reflects the rapid convergence typically associated with spectral methods. The close alignment of the solution curves with the reference trajectory emphasises the efficacy of the Chebyshev-Gauss-Lobatto collocation approach utilised in the MSRM formulation. The figure demonstrates that MSRM achieves significant accuracy with a limited number of collocation points and refinements of the subintervals. The increasing agreement with the reference solution as $\Delta\tau$ decreases illustrates the improved accuracy of the MSRM under temporal refinement.

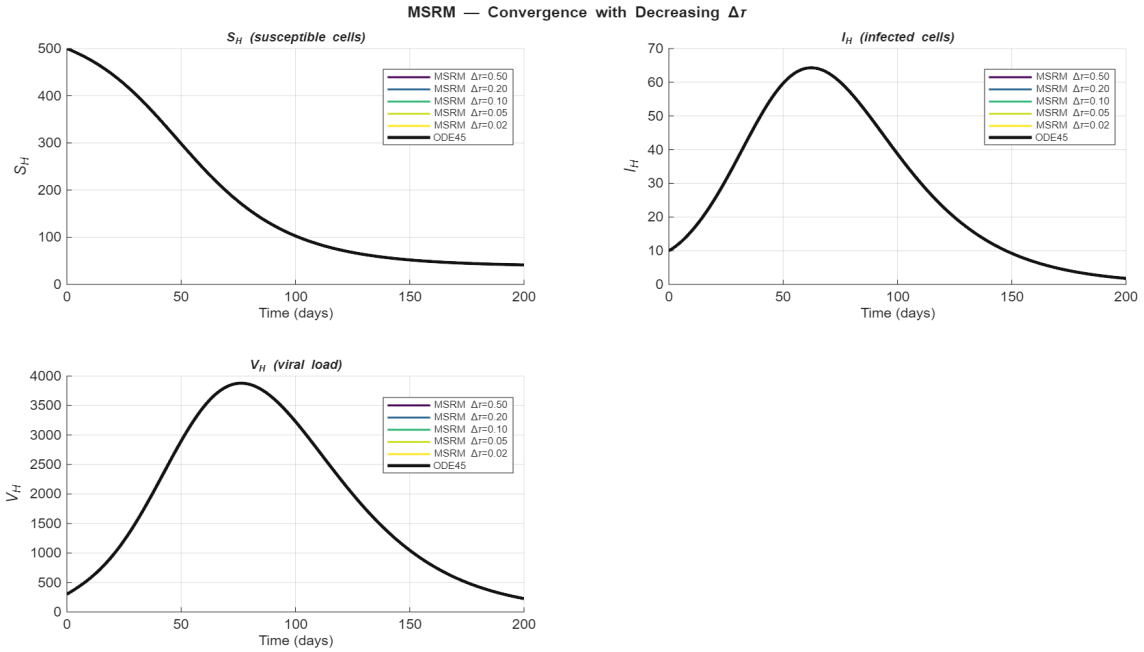


Figure 4. MSRM solutions for subinterval widths $\Delta\tau \in \{0.50, 0.20, 0.10, 0.05, 0.01\}$ compared with the ODE45 reference solution.

The observed convergence order is calculated from two successive discretisation parameters using

$$p \approx \frac{\log(E(h_1)/E(h_2))}{\log(h_1/h_2)}, \qquad h_1 > h_2, \tag{36}$$

where $E(h_i)$ denotes the relative L^2 error associated with the discretisation parameter h_i. For the MSRM, h_i in Equation (36) is replaced by the subinterval width $\Delta\tau_i$.

Tables 5 and 6 present the relative L^2 errors and the corresponding observed convergence orders for S_H, I_H, and V_H. For the NSFDM, the errors decrease approximately in proportion to the time-step size. The observed orders approach unity as h is refined; at $h = 0.01$, the orders are 0.99976, 0.99933, and 0.99931 for S_H, I_H, and V_H, respectively. These results confirm the expected first-order temporal convergence of the NSFDM for all three model variables. For the MSRM, the errors decrease much more rapidly. Over the range $\Delta\tau = 2.00$ to 0.10, the observed orders remain close to two, indicating an approximately second-order reduction in the measured global error over the coarse and intermediate refinements. When $\Delta\tau$ is reduced from 0.10 to 0.05, the errors fall sharply, producing larger apparent orders, particularly for S_H. These unusually large values should not be interpreted as a fixed algebraic convergence order; rather, they indicate that the MSRM is entering a very high-accuracy regime associated with the Chebyshev spectral approximation. At $\Delta\tau = 0.02$, the MSRM errors increase slightly relative to those obtained at $\Delta\tau = 0.05$, resulting in small negative observed orders. This does not indicate instability because the errors remain extremely small of order 10^{-9}–10^{-8} for S_H and 10^{-8}–10^{-7} for I_H and V_H. Instead, the computed order becomes unreliable once the discretisation error

approaches the numerical error floor determined by the ODE45 reference tolerance, the Gauss–Seidel stopping tolerance, interpolation, and floating-point round-off. Overall, the results show that the NSFDM is a consistent and robust first-order method, whereas the MSRM provides substantially smaller errors and rapid convergence. Therefore, the NSFDM remains attractive when positivity preservation and computational efficiency are the main priorities, while the MSRM is preferable when high numerical accuracy is required.

Table 5. Relative L^2 errors and observed convergence orders for the NSFDM.

h	E_{S_H}	p_{S_H}	E_{I_H}	p_{I_H}	E_{V_H}	p_{V_H}
2.00	6.7251×10^{-2}	−−	1.4171×10^{-1}	−−	1.4478×10^{-1}	−−
1.00	3.4229×10^{-2}	0.97432	7.4289×10^{-2}	0.93169	7.6012×10^{-2}	0.92960
0.50	1.7263×10^{-2}	0.98755	3.8032×10^{-2}	0.96593	3.8940×10^{-2}	0.96497
0.20	6.9403×10^{-3}	0.99446	1.5429×10^{-2}	0.98458	1.5804×10^{-2}	0.98415
0.10	3.4760×10^{-3}	0.99759	7.7510×10^{-3}	0.99322	7.9402×10^{-3}	0.99304
0.05	1.7394×10^{-3}	0.99881	3.8846×10^{-3}	0.99663	3.9796×10^{-3}	0.99653
0.02	6.9612×10^{-4}	0.99944	1.5561×10^{-3}	0.99844	1.5942×10^{-3}	0.99840

Table 6. Relative L^2 errors and observed convergence orders for the MSRM.

$\Delta\tau$	E_{S_H}	p_{S_H}	E_{I_H}	p_{I_H}	E_{V_H}	p_{V_H}
2.00	8.6852×10^{-5}	−−	2.7363×10^{-4}	−−	2.2167×10^{-4}	−−
1.00	2.1715×10^{-5}	1.9999	6.8426×10^{-5}	1.9996	5.5427×10^{-5}	1.9998
0.50	5.4286×10^{-6}	2.0001	1.7106×10^{-5}	2.0000	1.3855×10^{-5}	2.0002
0.20	8.6689×10^{-7}	2.0021	2.7312×10^{-6}	2.0023	2.2166×10^{-6}	2.0001
0.10	2.1026×10^{-7}	2.0437	6.6635×10^{-7}	2.0352	5.4412×10^{-7}	2.0263
0.05	3.2389×10^{-9}	6.0205	7.1052×10^{-8}	3.2293	9.0922×10^{-8}	2.5812

Figure 5 demonstrates that the relative L^2 errors decrease as the time discretisation parameters are refined. For the NSFDM, the error curves for S_H, I_H, and V_H are nearly parallel to the $\mathcal{O}(h)$ reference line, confirming approximately first-order convergence. The MSRM produces considerably smaller errors and follows an approximately $\mathcal{O}(\Delta\tau^2)$ trend over the coarse and intermediate subinterval widths. At very small values of $\Delta\tau$, the MSRM errors level off or increase slightly because the solution has reached a numerical error floor associated with the reference-solver tolerance, iteration tolerance, interpolation, and round-off errors. Overall, the graph confirms that the NSFDM achieves stable, consistent first-order convergence, whereas the MSRM achieves faster convergence and substantially greater accuracy.

Figures 6–10 examine the effects of varying key biological parameters on the infection dynamics.

Figure 6 shows that increasing the infection rate accelerates the transformation of susceptible cells into infected ones. Consequently, the quantity of susceptible cells declines at a faster rate, while the populations of infected cells and viral loads increase significantly. Both NSFDM and MSRM accurately reproduce the patterns observed in the ODE45 solutions. This indicates that the nonlinear dynamics resulting from the parameters are effectively captured.

Figure 7 shows that increasing values of δ_H enhance the rate at which infected cells are eliminated. This results in reduced populations of infected cells and decreased viral loads. The numerical results from NSFDM and MSRM align closely with the reference trajectories, demonstrating robustness under variations in parameters.

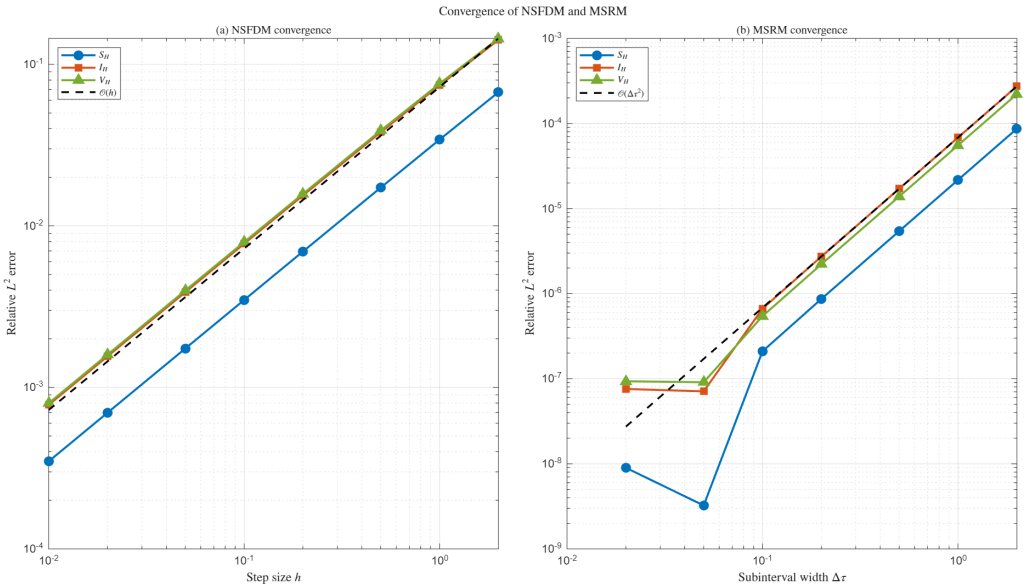


Figure 5. Log−log plots of the relative errors in S_H, I_H, and V_H as functions of the temporal discretisation parameter with the NSFDM using the step size h, whereas the MSRM uses the subinterval width $\Delta\tau$.

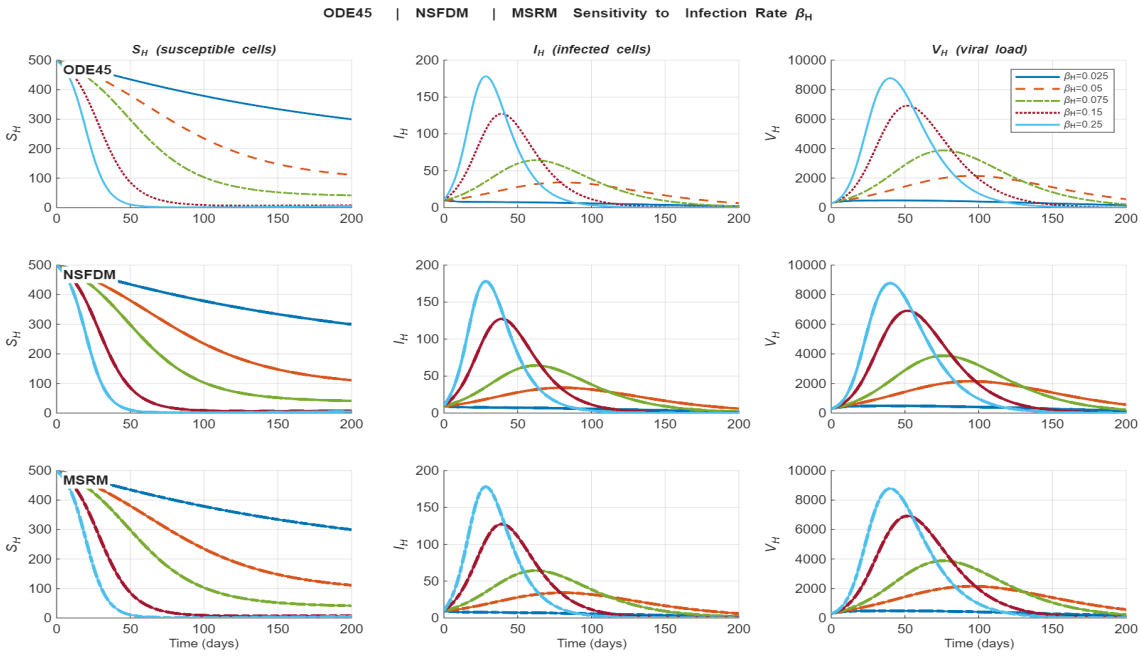


Figure 6. Sensitivity of the numerical solutions S_H, I_H, and V_H to variations in the human-to-human transmission rate $\beta_H \in \{0.025, 0.050, 0.075, 0.150, 0.250\}$. The results obtained using the NSFDM and MSRM are compared with the ODE45 reference solutions. The NSFDM was implemented with $h = 0.01$, while the MSRM used $\Delta\tau = 0.10$ and $N_{\text{ch}} = 8$.

Figure 8 shows that increasing the viral clearance rate μ_V reduces both the viral load V_H and the infected host population I_H, while preserving a larger susceptible population S_H. Low values of μ_V lead to prolonged viral persistence and a more severe outbreak, whereas high values suppress viral accumulation and infection. The NSFDM and MSRM solutions agree closely with the ODE45 reference solution, confirming that both methods accurately capture the model's sensitivity to μ_V.

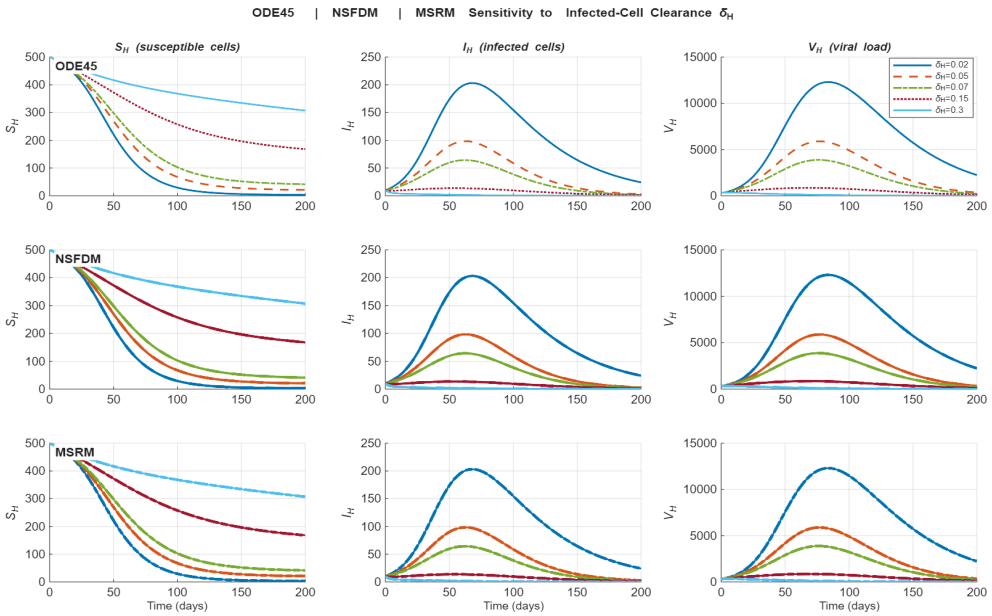


Figure 7. Sensitivity of the numerical solutions S_H, I_H, and V_H to variations in the infected-host removal rate $\delta_H \in \{0.02, 0.05, 0.07, 0.15, 0.30\}$. The NSFDM and MSRM solutions are compared with the ODE45 reference solutions. The NSFDM was implemented using $h = 0.01$, while the MSRM used $\Delta\tau = 0.10$ and $N_{\text{ch}} = 8$.

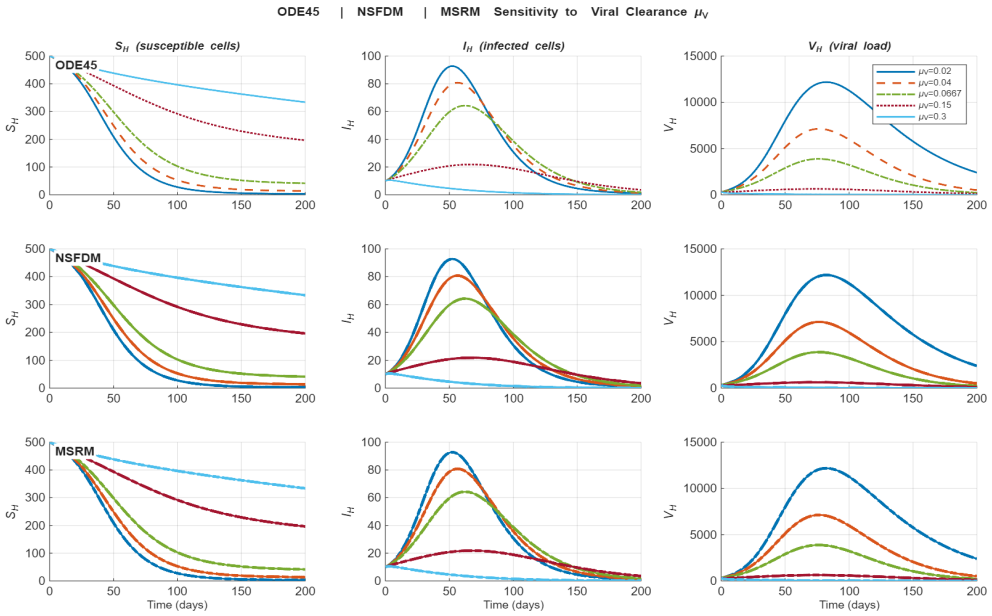


Figure 8. Sensitivity of the numerical solutions S_H, I_H, and V_H to variations in the infected-host removal rate $\mu_V \in \{0.02, 0.04, 0.0667, 0.15, 0.30\}$. The NSFDM and MSRM results are compared with the ODE45 reference solutions, with the NSFDM implemented using a time-step size of $h = 0.01$.

Figure 9 shows that an increase in α_h enhances the production of viruses from infected cells. This leads to greater viral peaks and more intense infection patterns. This response is reliably observed across all numerical techniques.

Figure 10 shows that increasing the natural host death rate μ_H accelerates the decline of both the susceptible population S_H and the infected population I_H. Consequently, the viral load V_H also decreases because fewer infected hosts remain available to produce and shed the virus. The close agreement among NSFDM, MSRM, and ODE45 confirms that both numerical schemes accurately capture the sensitivity of the model to variations in

μ_H. The strong correlation observed between NSFDM, MSRM, and ODE45 indicates an accurate representation of clearance dynamics.

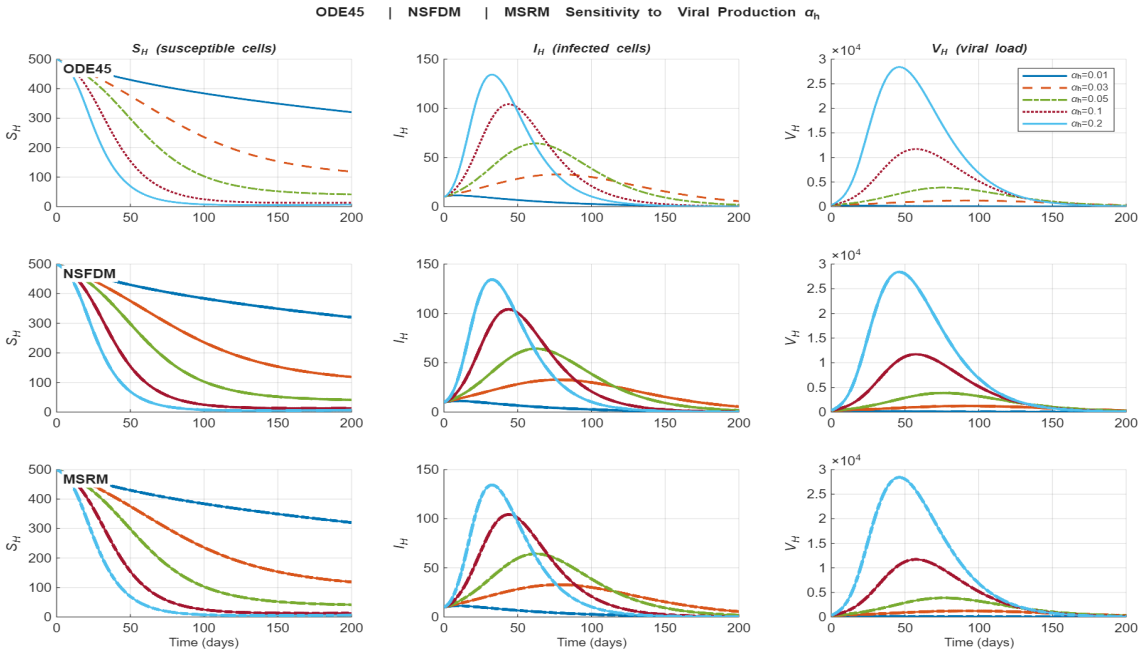


Figure 9. Sensitivity of the numerical solutions S_H, I_H, and V_H to variations in the Norovirus shedding rate $\alpha_h \in \{0.01, 0.03, 0.05, 0.10, 0.20\}$. The solutions obtained using the NSFDM and MSRM are compared with the ODE45 reference solutions. The NSFDM was implemented using a time-step size of $h = 0.01$.

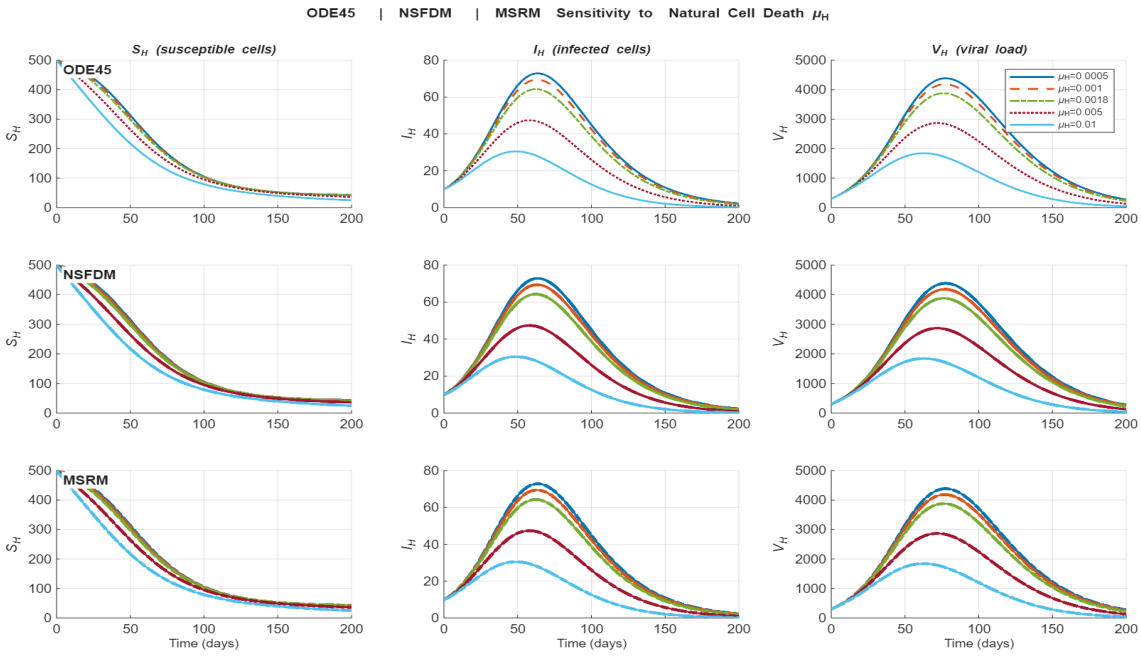


Figure 10. Sensitivity of the numerical solutions S_H, I_H, and V_H to variations in the natural host mortality rate $\mu_H \in \{0.0005, 0.0010, 0.0018, 0.0050, 0.0100\}$. The NSFDM and MSRM solutions are compared with the ODE45 reference solutions. The NSFDM was implemented using a time-step size of $h = 0.01$.

The analysis of CPU times in Figure 11 and Table 7 indicates that NSFDM typically requires fewer computational resources due to its straightforward explicit-update format. Conversely, MSRM employs spectral collocation matrices and iterative Gauss-Seidel relax-

ations, which result in higher computational expense. Nevertheless, the enhanced costs associated with MSRM are justified by significantly better accuracy and quicker convergence rates. Therefore, NSFDM is an excellent option when computational efficiency and positivity preservation are top priorities. In contrast, MSRM is preferable when achieving high accuracy is critical.

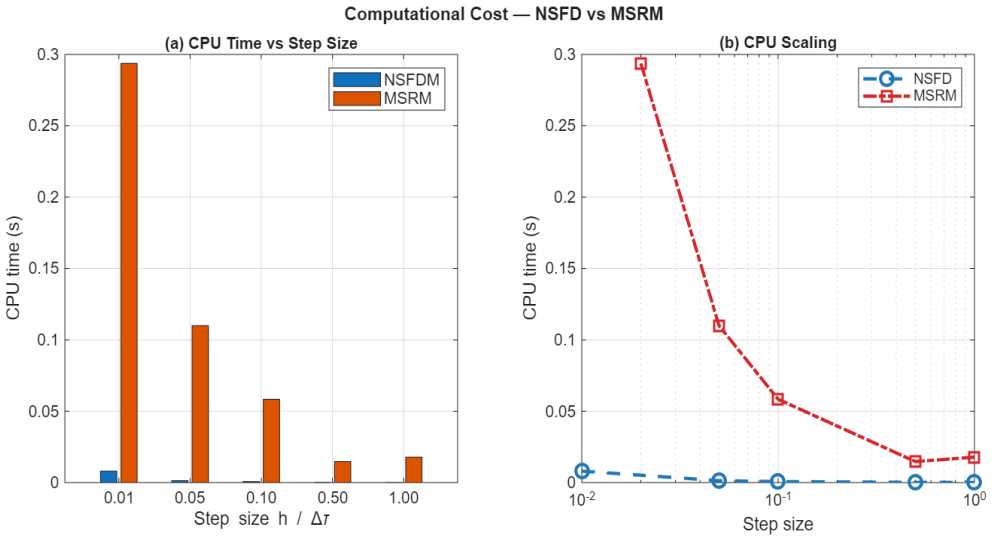


Figure 11. Computational Cost NSFDM vs. MSRM.

Table 7. Computational-time comparison between the NSFDM and MSRM for different temporal step sizes. The CPU times are measured in seconds.

Step Size, h or $\Delta\tau$	NSFDM CPU Time (s)	MSRM CPU Time (s)
0.01	8.52×10^{-3}	2.94×10^{-1}
0.05	1.83×10^{-3}	1.11×10^{-1}
0.10	1.43×10^{-3}	5.89×10^{-2}
0.50	6.50×10^{-4}	1.52×10^{-2}
1.00	6.50×10^{-4}	1.84×10^{-2}

6. Conclusions

This study examined the numerical solution of a nonlinear multiscale model of Norovirus infection using the nonstandard finite-difference method (NSFDM) and the multistage spectral relaxation method (MSRM). The two methods were assessed against an adaptive ODE45 reference solution for their ability to reproduce the model dynamics, maintain biologically meaningful solutions, achieve numerical accuracy, and control computational cost. The results show that both methods capture the main features of the infection process, including the decline in the susceptible population, the transient growth of the infected population, and the corresponding rise and subsequent reduction in the viral load. The NSFDM offers clear advantages when preserving the model's qualitative behaviour is a primary concern. Across the numerical experiments considered, the method produced non-negative, bounded approximations for all state variables, even at relatively large time steps. This is particularly important in epidemiological modelling, where negative population densities or viral concentrations are not biologically meaningful. The NSFDM is also straightforward to implement, since the numerical solution is obtained through sequential update formulas rather than repeated solutions of large algebraic systems. As a result, it requires substantially less computational time than the MSRM. These features make the NSFDM well-suited to long-time simulations, repeated parameter studies, sensitivity analyses, and applications in which computational efficiency and biological

consistency are essential. The main strength of the MSRM lies in its numerical accuracy. By combining Chebyshev–Gauss–Lobatto collocation, temporal domain decomposition, and Gauss–Seidel-type relaxation, the method provides accurate approximations on each subinterval and closely follows the ODE45 reference solution. The error results indicate that the MSRM generally produces smaller numerical errors than the NSFDM, particularly in regions where the solution changes rapidly, such as near the peak of the viral load. This makes the MSRM attractive for high-fidelity simulations, benchmark computations, parameter estimation, model calibration, and other applications where small numerical errors can influence the interpretation of results. The comparison also reveals an important trade-off between accuracy and computational cost. The improved accuracy of the MSRM is achieved at the expense of additional computational effort due to the construction of spectral differentiation matrices, the repeated solution of linear algebraic systems, and the iterative relaxation process within each temporal subinterval. In contrast, the NSFDM is computationally economical and remains reliable over a wider range of step sizes. The preferred method, therefore, depends on the purpose of the simulation: the NSFDM is advantageous when robustness, efficiency, and biologically admissible solutions are required, whereas the MSRM is more appropriate when high numerical precision is the main priority. The present study is primarily computational. Although the numerical experiments suggest that the NSFDM preserves positivity and boundedness and that the MSRM converges rapidly to the reference solution, complete analytical proofs of positivity, stability, boundedness, and convergence have not been provided. This is an important limitation and should be addressed in future work. Further studies may also consider higher-order NSFDM formulations, adaptive selection of the MSRM subinterval length and collocation points, and efficient implementations that reduce the computational cost of the spectral method. Overall, the NSFDM and MSRM should be viewed as complementary rather than competing approaches. The NSFDM provides an efficient and biologically consistent framework for large-scale, long-term simulations, while the MSRM offers greater numerical accuracy for applications that require high-resolution approximations. Their combined assessment provides a useful basis for selecting numerical methods for nonlinear multiscale infectious-disease models and for extending the present framework to more detailed models that incorporate environmental transmission, spatial movement, treatment, vaccination, stochastic effects, or optimal control.

Funding: The author gratefully acknowledges the financial support provided by the University of Venda.

Data Availability Statement: No new data were created or analysed in this study. Data sharing is not applicable to this article.

Conflicts of Interest: The author declares that there is no conflict of interest regarding the publication of this paper.

Abbreviations

The following abbreviations are used in this manuscript:

MSRM	Multistage Spectral Relaxation Method
SRM	Spectral Relaxation Method
NSFDM	Nonstandard Finite Difference Method
ODE	Ordinary Differential equations
CPU	Central Processing Unit
HIV/AIDS	Human Immunodeficiency Virus/Acquired Immunodeficiency Syndrome
ODE45	Runge–Kutta Method of order 5(4)
CGL	Chebyshev–Gauss–Lobatto

References

1. Heesterbeek, H.; Anderson, R.M.; Andreasen, V.; Bansal, S.; De Angelis, D.; Dye, C.; Eames, K.T.D.; Edmunds, W.J.; Frost, S.D.W.; Funk, S.; et al. Modeling infectious disease dynamics in the complex landscape of global health. *Science* **2015**, *347*, aaa4339. [CrossRef]
2. Garira, W. A complete categorisation of multiscale models of infectious disease systems. *J. Biol. Dyn.* **2017**, *11*, 378–435. [CrossRef] [PubMed]
3. Garira, W.; Muzhinji, K. Application of the replication–transmission relativity theory in the development of multiscale models of infectious disease dynamics. *J. Biol. Dyn.* **2023**, *17*, 2255066. [CrossRef] [PubMed]
4. Garira, W. The replication-transmission relativity theory for multiscale modelling. *Sci. Rep.* **2019**, *9*, 16353. [CrossRef] [PubMed]
5. Garira, W. A primer on multiscale modelling of infectious disease systems. *Infect. Dis. Model.* **2018**, *3*, 176–191. [PubMed]
6. Garira, W.; Mathebula, D. Development and application of multiscale models of acute viral infections. *Math. Methods Appl. Sci.* **2020**, *43*, 3280–3306.
7. Netshikweta, R.; Garira, W. A nested multiscale model to study paratuberculosis in ruminants. *Front. Appl. Math. Stat.* **2022**, *8*, 817060. [CrossRef]
8. Hoang, M.T.; Ehrhardt, M. Differential equation models for infectious diseases: Mathematical modeling, qualitative analysis, numerical methods and applications: MT Hoang, M. Ehrhardt. *SeMA J.* **2025**, 1–36. [CrossRef]
9. Movaheedi, Z.; Khapulwak, S.; Faqiri, R. A Comparative Study of Nonstandard Finite Difference (NSFD) and Classical Methods for a Tuberculosis Susceptible–Infected–Recovered (SIR) Model. *Spinghar J. Biomed. Sci.* **2026**, *2*, 103–120. [CrossRef]
10. Adel, M.; Khader, M.M.; Ahmad, H.; Oqilat, O.; Abdelfattah, W.M. Using the Multi-Domain Spectral Relaxation Method through a Numerical Simulation for the Brusselator System. *Eur. J. Pure Appl. Math.* **2025**, *18*, 7064. [CrossRef]
11. Magagula, V. M. On the multidomain bivariate spectral local linearisation method for solving systems of nonsimilar boundary layer partial differential equations. *Int. J. Math. Math. Sci.* **2019**, *2019*, 6423294. [CrossRef]
12. Motsa, S.S.; Shateyi, S. Successive linearisation analysis of unsteady heat and mass transfer from a stretching surface embedded in a porous medium with suction/injection and thermal radiation effects. *Can. J. Chem. Eng.* **2012**, *90*, 1323–1335.
13. Awad, F.G.; Motsa, S.; Khumalo, M. Heat and mass transfer in unsteady rotating fluid flow with binary chemical reaction and activation energy. *PLoS ONE* **2014**, *9*, e107622. [CrossRef] [PubMed]
14. Mickens, R.E. *Advances in Applications of Nonstandard Finite Difference Schemes*; World Scientific: Singapore, 2005.
15. Marime, C.B.; Munyakazi, J.B. A second-order nonstandard finite difference method for a malaria propagation model with control. *AppliedMath* **2026**, *6*, 36. [CrossRef]
16. Morani, A.H.; Saeed, M.M.; Aslam, M.; Mehmoud, A.; Shokri, A.; Mukalazi, H. Local and global stability analysis of HIV/AIDS by using a nonstandard finite difference scheme. *Sci. Rep.* **2025**, *15*, 4502. [CrossRef] [PubMed]
17. Maamar, M.H.; Ehrhardt, M.; Tabharit, L. A nonstandard finite difference scheme for a time-fractional model of Zika virus transmission. *Math. Biosci. Eng.* **2024**, *21*, 924–962. [CrossRef] [PubMed]
18. Anguelov, R.; Lubuma, J.M.S. Contributions to the mathematics of the nonstandard finite difference method and applications. *Numer. Methods PDEs* **2001**, *17*, 518–543. [CrossRef]
19. Garba, S.M.; Gumel, A.B.; Lubuma, J.S. Dynamically-consistent non-standard finite difference method for an epidemic model. *Math. Comput. Model.* **2011**, *53*, 131–150. [CrossRef]
20. Lubuma, J.S.; Mureithi, E.; Terefe, Y.A. Analysis and dynamically consistent numerical schemes for the SIS model and related reaction diffusion equation. *AIP Conf. Proc.* **2011**, *1404*, 168–175. [CrossRef]
21. Mickens, R.E. Nonstandard finite difference schemes for differential equations. *J. Differ. Equ. Appl.* **2002**, *8*, 823–847. [CrossRef]
22. Maphiri, A.D.; Muzhinji, K.; Mathebula, D.; Netshikweta, R. Multiscale modeling of norovirus in humans. *J. Biol. Syst.* **2025**, *33*, 1419–1454. [CrossRef]
23. Handel, A.; Rohani, P. Crossing the scale from within-host infection dynamics to between-host transmission fitness: A discussion of current assumptions and knowledge. *Philos. Trans. R. Soc. B Biol. Sci.* **2015**, *370*, 20140301. [CrossRef] [PubMed]
24. Namawejje, H.; Luboobi, L.S.; Kuznetsov, D.; Wobudeya, E. Mathematical model for the effects of treatment and vaccination controls on the dynamics of rotavirus disease with reference to Uganda. *J. Math. Comput. Sci.* **2014**, *4*, 958–991
25. Trefethen, L.N. *Spectral Methods in MATLAB*; SIAM: Philadelphia, PA, USA, 2000.
26. Canuto, C.; Hussaini, M.Y.; Quarteroni, A.; Zang, T.A. *Spectral Methods*; Springer: Berlin, Germany, 2006; Volume 285.
27. Motsa, S.S. A new spectral relaxation method for similarity variable nonlinear boundary layer flow systems. *Chem. Eng. Commun.* **2014**, *201*, 241–256. [CrossRef]
28. Motsa, S.S.; Dlamini, P.G.; Khumalo, M. Solving hyperchaotic systems using the spectral relaxation method. *Abstr. Appl. Anal.* **2012**, *2012*, 203461. [CrossRef]
29. Motsa, S.S.; Magagula, V.M.; Sibanda, P. A bivariate Chebyshev spectral collocation quasilinearization method for nonlinear evolution parabolic equations. *Sci. World J.* **2014**, *1*, 581987. [CrossRef] [PubMed]
30. Mickens, R.E. *Nonstandard Finite Difference Models of Differential Equations*; World Scientific: Singapore, 1994.

31. Anguelov, R.; Lubuma, J.M.S. Nonstandard finite difference method by nonlocal approximation. *Math. Comput. Simul.* **2003**, *61*, 465–475. [CrossRef]
32. González-Parra, G.; Arenas, A.J.; Chen-Charpentier, B.M. Combination of nonstandard schemes and Richardson's extrapolation to improve the numerical solution of population models. *Math. Comput. Model.* **2010**, *52*, 1030–1036. [CrossRef]
33. Patidar, K.C. Nonstandard finite difference methods: Recent trends and further developments. *J. Differ. Equ. Appl.* **2016**, *22*, 817–849. [CrossRef]

Disclaimer/Publisher's Note: The statements, opinions and data contained in all publications are solely those of the individual author(s) and contributor(s) and not of MDPI and/or the editor(s). MDPI and/or the editor(s) disclaim responsibility for any injury to people or property resulting from any ideas, methods, instructions or products referred to in the content.